nature astronomy

Article

https://doi.org/10.1038/s41550-024-02402-9

A super-Eddington-accreting black hole ~1.5 Gyr after the Big Bang observed with JWST

Received: 1 April 2024

Accepted: 1 October 2024

Published online: 04 November 2024

Check for updates

Hyewon Suh[1] ✉, Julia Scharwächter[1], Emanuele Paolo Farina[1], Federica Loiacono[2], Giorgio Lanzuisi[2], Günther Hasinger[3,4,5], Stefano Marchesi[2,6,7], Mar Mezcua[8,9], Roberto Decarli[2], Brian C. Lemaux[1,10], Marta Volonteri[11], Francesca Civano[12], Sukyoung K. Yi[13], San Han[13], Mark Rawlings[1] & Denise Hung[1]

Recent James Webb Space Telescope (JWST) observations have revealed a surprisingly abundant population of faint, dusty active galactic nuclei at $z \approx 4$–7. Together with the presence of supermassive black holes at $z > 6$, this raises questions about the formation and growth histories of early black holes. Current theories for the formation of seed black holes from the death of the first stars (that is, light seeds) and/or the direct collapse of primordial gas clouds (that is, heavy seeds) still lack observational confirmation. Here we present LID-568, a low-mass ($7.2 \times 10^6\,M_\odot$) black hole hosting powerful outflows that is observed in an extreme phase of rapid growth at redshift $z \approx 4$. This object is similar to other JWST-discovered faint active galactic nuclei populations, but is bright in X-ray emission and accreting at more than 4,000% of the limit at which radiation pressure exceeds the force of gravitational attraction of the black hole (that is, super-Eddington accretion). Analysis of JWST Near-Infrared Spectrograph integral field unit data reveals spatially extended Hα emission with velocities of ~−600−−500 km s^{-1} relative to the central black hole, indicative of robust nuclear-driven outflows. LID-568 represents an elusive low-mass black hole experiencing super-Eddington accretion as invoked by models of early black hole formation. This discovery showcases a previously undiscovered key parameter space and offers crucial insights into rapid black hole growth mechanisms in the early universe.

Observational surveys have identified several hundreds of luminous quasars at redshift $z > 6$–7 (refs. 1–6). The presence of supermassive black holes (SMBHs) with masses of $10^{9-10}\,M_\odot$ at such early cosmic epochs challenges models of SMBH formation and growth, and raises questions about the origin of seed black holes and the mechanisms for their rapid and extreme growth. Although the formation of seed black holes remains observationally unconstrained, they are commonly thought to originate in the first galaxies through several gas or stellar physical processes that can generate black holes with masses in excess of $10^2\,M_\odot$ (ref. 7). Historically, models have been divided into light and heavy seeds, with a demarcation at about $10^3\,M_\odot$. The lightest seeds are generally associated with the death of the first stars with initial masses of $10^{2-3}\,M_\odot$ (refs. 8,9). The growth of such light seeds at very early time into the observed population of SMBHs at slightly later time is challenging, because black holes formed in this manner would have to accrete at the Eddington limit from the time they are formed up to the redshift

A full list of affiliations appears at the end of the paper. ✉e-mail: hyewon.suh@noirlab.edu

https://doi.org/10.1038/s41550-024-02402-9

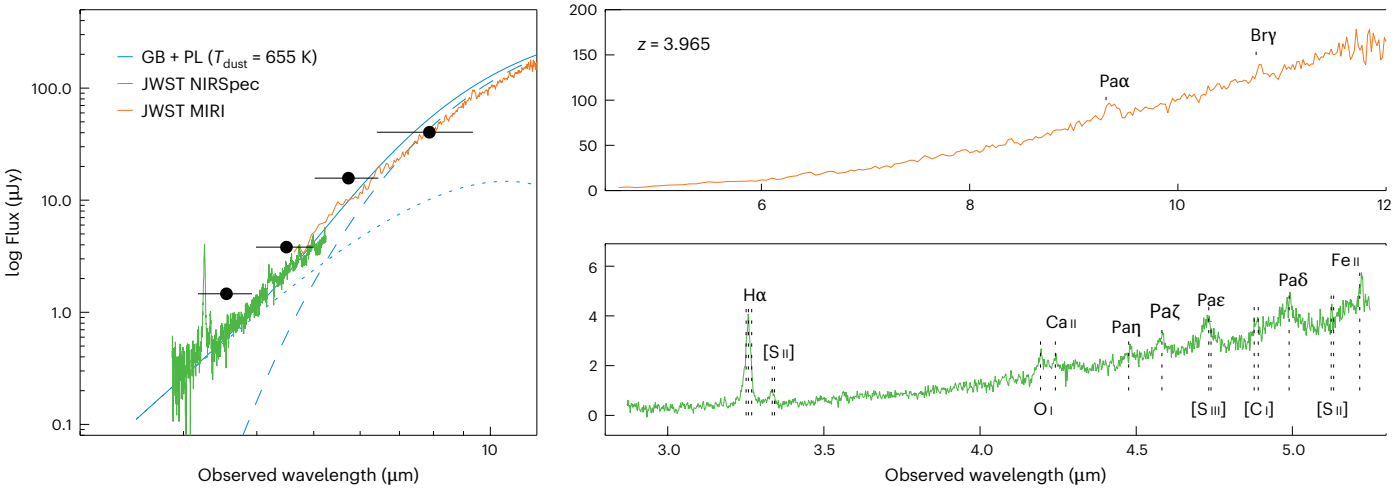

Fig. 1 | The NIRSpec and MIRI spectra of LID-568. Left: Spitzer/IRAC 3.6, 4.5, 5.8 and 8.0 μm photometry (black points) with the best-fitting SED model (blue), including a power law (blue dotted) and greybody (blue dashed) components, at a spectroscopic redshift of z_{spec} = 3.965 (Methods). The horizontal error bars represent the filter bandwidth. The JWST NIRSpec (green) and MIRI (orange) spectra are overplotted. Right: the spectra of LID-568 obtained with MIRI (top) and NIRSpec (bottom), with the detected emission lines marked.

at which they are observed[10], which appears to be difficult[11]. The direct collapse of primordial gas clouds into supermassive stars turning into black holes with initial masses of 10^{4-6} $M_{\odot}$ (that is, heavy seed)[12,13] is an attractive alternative, as these heavy seeds can more rapidly grow into SMBHs even by means of slightly sub-Eddington accretion. However, the expected number densities for the sites where such supermassive stars can form are low. Intermediate pathways where seeds of 10^{3-4} $M_{\odot}$ form from very massive stars in pristine rapidly growing halos or through stellar mergers, hierarchical black hole mergers and stellar captures in dense stellar systems bridge these two extremes[14]. It is also possible that heavy seeds originate from primordial black holes, eliminating the need for the stellar and gas-based processes[15–17].

With the unprecedented sensitivity of the James Webb Space Telescope (JWST), it is now possible to extend studies to faint, low-mass sources at high redshifts (that is, $z > 3$–4), an epoch when both black holes and galaxies are still rapidly growing their mass, and such observation can provide insights into the mechanisms seeding early black holes. JWST has recently discovered a new population of relatively faint, compact, dust-reddened sources at $z > 4$ using various selection techniques in a wide variety of extragalactic surveys[18–24]. They are found to have overmassive black holes with respect to the local black hole mass (M_{BH})–stellar mass ($M_{stellar}$) relationship, exhibiting 10–100 times higher $M_{BH}/M_{stellar}$ ratios[25]. Most of these sources have not been detected in X-ray observations[18–24]; only two sources with X-ray-detections have been recently reported[26]. This faint population is likely to represent the moderate accretion phase of active galactic nuclei (AGNs), which are accreting at ~20% of the Eddington rates, and are hosted by relatively low-mass galaxies. Some of these sources are referred to as 'little red dots' and are characterized by a red continuum in the rest-frame optical and a modest blue UV continuum. Such sources exhibit prominent broad Balmer emission lines, which implies that they are powered by AGNs. These red compact sources are surprisingly abundant, being 100 times more common than UV-selected quasars at similar redshifts[23].

LID-568, an X-ray AGN, was discovered among a hidden black hole population identified as near-infrared-dropout (near-IR-dropout) X-ray sources from the Chandra-COSMOS Legacy Survey[27,28]. Similar to other faint AGNs discovered by JWST, LID-568 appears extremely red and compact in the IR, yet it remains invisible in any optical wavelengths and even in the deepest near-IR imaging taken with the Hubble Space Telescope (HST). Its spectroscopic redshift, z_{spec} = 3.965, was determined from JWST Near-Infrared Spectrograph (NIRSpec) and (Mid-Infrared Instrument (MIRI) observations, based on broad Hα, [S II]

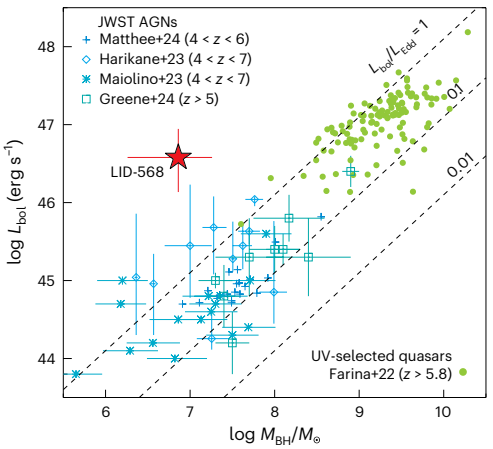

Fig. 2 | AGN bolometric luminosity (L_{bol}) versus black hole mass (M_{BH}) of AGNs at high redshift. LID-568, with super-Eddington accretion ($L_{bol}/L_{Edd} \approx 41.5$) at $z \approx 4$, is shown as a red star. Its X-ray-derived bolometric luminosity is approximately a factor of 100 higher than that of faint AGNs at $z \approx 4$–7 with low-mass black holes[18,20,23,24] recently found by JWST observations. For reference, UV-selected quasars[5] at $z > 5.8$ are also shown. Systematic uncertainties on M_{BH} associated with different single-epoch virial calibrations typically have a scatter of ~0.3 dex. Error bars represent 1σ uncertainties.

and Paschen emission lines. The NIRSpec and MIRI spectra of LID-568 are shown in Fig. 1. However, LID-568 stands out as uniquely bright in the X-ray region relative to the population of faint AGNs discovered by JWST, which indicates a higher level of central accretion activity. The observed 0.5–10 keV flux is 5.16×10^{-15} erg cm^{-2} s^{-1} (ref. 27). Analysis of the X-ray spectrum (as inferred from the emission measured in the 0.5–2 keV and 2–7 keV bands) allows us to measure the obscuration (hydrogen column density, log N_H = 23.44 (−0.34 + 0.47) cm^{-2}) and the absorption-corrected luminosity in the 0.5–10 keV band (Methods). The absorption-corrected X-ray luminosity suggests an AGN bolometric luminosity of log L_{bol} = 46.6 (−0.44 + 0.36) erg s^{-1}, a factor of ~100 higher than the average bolometric luminosities of JWST-discovered faint AGNs.

The shape of the mid- to far-IR spectral energy distribution (SED) of LID-568 exhibits an extremely red IR continuum slope with a single power law of $\alpha_{\lambda} \approx 4.5$ at $\lambda_{rest} \gtrsim 1$ μm (Extended Data Fig. 1). This characteristic cannot be explained by the currently available IR SED templates

https://doi.org/10.1038/s41550-024-02402-9

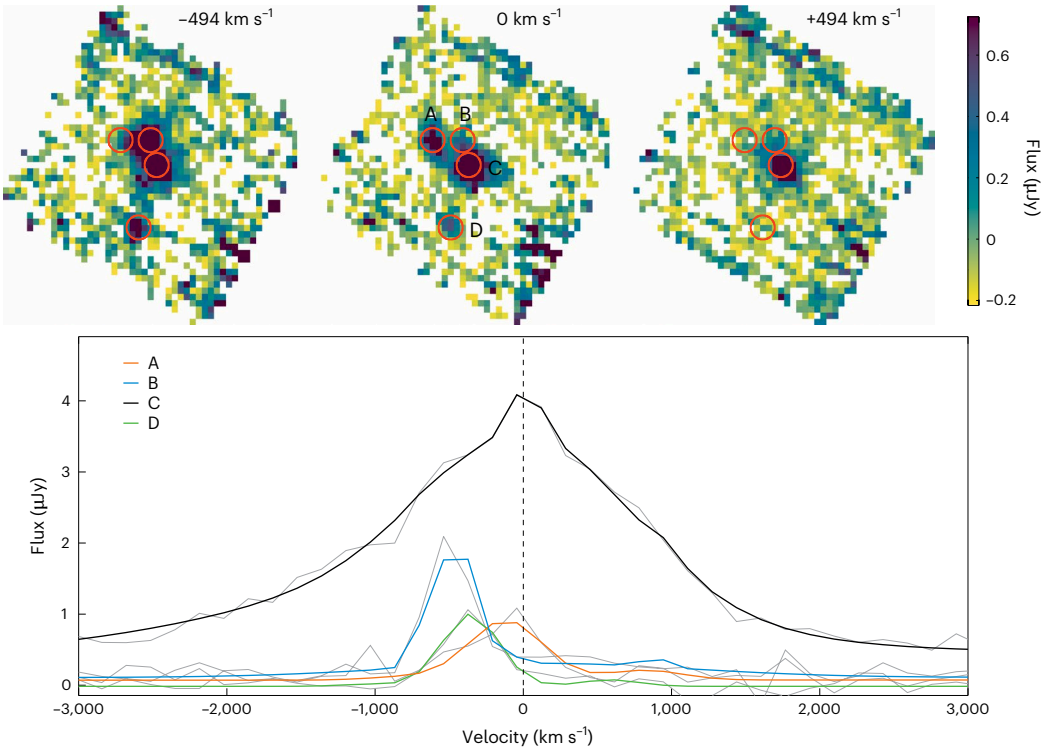

Fig. 3 | JWST NIRSpec/IFU channel maps for the Hα emission line region. Top: each map shows the Hα emission line fluxes in different velocity bins. The spatially extended outflow components B and D are at velocity offsets of ~−600–−500 km s^{-1} with respect to the central broad-line component (C), whereas component A is found at a similar velocity to component C. Bottom: NIRSpec spectra of each component are shown in the Hα emission line region, extracted from circular apertures with a radius of 0.2″.

for obscured AGN and ultraluminous infrared galaxies (ULIRGs) and is substantially steeper than those of the faint AGNs discovered by JWST (which exhibit a power-law slope $\alpha_\lambda \approx 2.0$ on average)[19]. The detection of X-ray and mid-IR emission strongly suggests that LID-568 is indeed a heavily obscured AGN, without an apparent presence of the underlying host galaxy features. The model SEDs for super-Eddington accretion suggest a notable absence of rest-frame UV or even optical emission, with a tendency to become progressively redder in the IR as the Eddington ratio increases[29]. However, contrasting perspectives have been presented in other studies, indicating that super-Eddington accretion might lead to an excess of UV radiation, resulting in a significantly bluer continuum slope in the rest-frame UV[30,31].

Given the point-like, compact nature of this source, the extremely red colour primarily arises from the thermal emission originating in a dust-obscured accretion disk, with negligible contribution from a host galaxy. Based on IR SED fitting that employs a power law and two greybodies[32] (Methods and Extended Data Fig. 1), the dust temperature is substantially higher (655.53 K and 71.5 K) than what is typically observed in star-forming galaxies (10–60 K). This indicates that hot and warm gas dominates the IR emission, with negligible evidence of star formation activity. This is in contrast to the majority of dust-obscured galaxies at high redshift, which often exhibit signs of powerful starbursts. The derived total IR luminosity is $\log L_{8\text{–}1{,}000\,\mu m} \approx 46.1$ erg s^{-1}, which is comparable to the AGN bolometric luminosity. The estimated dust mass M_{dust} is ~$2.95 \times 10^6\,M_\odot$, which suggests that LID-568 contains less dust than the optically faint, dust-obscured galaxies at $z \approx 3$ (that is, H-dropouts, HST-dark, NIR-dark)[33,34] that have dust masses of ~$1–4 \times 10^8\,M_\odot$. Assuming the dust-to-stellar mass ratios of HST-dark, dust-obscured galaxies at similar redshifts[33], the inferred stellar mass of LID-568 is ~$2 \times 10^8\,M_\odot$, which implies a low-mass (that is, dwarf) galaxy.

The single-epoch virial black hole mass (M_{BH}), derived from the broad Hα emission line, is $7.2\,(-5.4 + 10.8) \times 10^6\,M_\odot$, which indicates a rather low-mass black hole (Methods and the left panel of Extended Data Fig. 2). This yields an Eddington ratio (L_{bol}/L_{Edd}) of 41.5, which implies extreme super-Eddington accretion activity. In Fig. 2, we show that the black hole mass of LID-568 is comparable with those of faint AGNs discovered by JWST at $z \approx 4–7$. However, the notably higher bolometric luminosity of this object places it within a previously unexplored extreme accretion regime. On the other hand, there is growing evidence that AGNs with high accretion rates appear to have smaller broad-line region (BLR) sizes than those predicted by the canonical radius–luminosity relationship of sub-Eddington AGNs[35,36]. This discrepancy could potentially lead to an overestimation of the single-epoch black hole mass by as much as ~0.3 dex, resulting in a higher Eddington ratio.

The ionized gas in LID-568 shows signs of a spatially unresolved nuclear outflow with velocities of ~−540 km s^{-1} (Methods and the right panel of Extended Data Fig. 2), which are similar to the velocities traced by the spatially extended Hα emission. In Fig. 3, we present NIRSpec/Integral Field Unit (IFU) channel maps of the Hα emission at different velocity ranges chosen to best highlight the multiple kinematic components observed around the central black hole (Extended Data Fig. 3). The blue-shifted Hα emission (~−600–−500 km s^{-1}) peaks at a projected distance of 0.4″ (~3 kpc) to the north (B component) and 1″ (~7 kpc) towards the south (D component) from the central broad-line component (C component), whereas the north-eastern component A is found at a similar velocity to the central component C. The continuum emission associated with the spatially extended Hα emission components are not detected. Although these components could be part of the outflow, a merger origin cannot be excluded.

If the extended Hα emissions are associated with outflows, we can infer the AGN lifetime using the outflow velocity and radius. Considering that the outflow reaches ~7 kpc from the central black hole, we obtain the AGN lifetime as $t = (7\text{ kpc})/(540\text{ km s}^{-1}) \approx 1.2 \times 10^7$ yr. This lifetime is consistent with the lower limits on total accretion timescales set by Soltan arguments (that is, $10^{7–9}$ yr (ref. 37)) and indirect measurements of AGN phase timescales (~$10^{7–9}$ yr (ref. 38)). Furthermore,

theoretical studies[39] suggest that super-Eddington phases might be sustained over timescales of a few tens of million years. This lifetime suggests that a substantial fraction of the mass growth of LID-568 may have occurred in a single, super-Eddington accretion episode.

To estimate the preburst mass of the black hole, we calculated the mass growth during super-Eddington accretion over 12 Myr using the equation $M_{BH}(t-t_0)/M_{BH}(t_0) = \exp((1-\epsilon)\lambda_{Edd}(t-t_0)/(\epsilon \times t_{Edd}))$, where $t_{Edd} = 450$ Myr and the radiative efficiency ϵ is 0.1. The estimated black hole mass before super-Eddington accretion is ~10^2 $M_\odot$ (that is, light seed). We note that this growth scenario is feasible only if the black hole remains embedded within a giant molecular cloud and accretes the entire cloud without substantially altering the Bondi radius due to feedback. As such, this represents a lower limit on the pre-accretion black hole mass, which is consistent with a light seed but does not exclude the possibility of a more nuanced growth history with shorter accretion events happening on a heavier seed. In fact, it is also possible that the outflow could be associated with stellar feedback-driven outflows from a starburst event preceding the activity in the black hole.

The presence of potentially AGN-driven outflows, along with the lack of star-forming activity in LID-568, suggests that AGN feedback may play a crucial role in regulating and/or quenching star formation in this low-mass system at high redshift. This indicates the possibility of rapid and efficient growth of black holes relative to their host galaxies. Theoretical models predict a 'blowout' dusty red quasar phase transitioning from a heavily obscured starburst, during which AGN-driven outflows eject gas and dust from the host galaxy, thereby quenching the star formation[40]. It is possible that LID-568 represents a transient phase characterized by extremely high accretion rates with powerful outflows suppressing the star formation in its host galaxy. This could explain the presence of overmassive black holes hosted in low-mass galaxies in the local Universe[41], as well as those found by JWST at $z > 4$ (ref. 25). Furthermore, the powerful AGN could produce dust in outflowing winds from the BLR (that is, smoking quasar)[42], and this could potentially account for the abundant dusty AGNs observed with JWST at high redshifts.

LID-568 could potentially represent the long-sought-after low-mass black hole undergoing rapid growth through super-Eddington accretion. The discovery of a super-Eddington accreting black hole at $z \approx 4$ unveils a missing key parameter space of the extreme accretion and provides new insights into the rapidly growing mechanisms of the early growth of black holes[43–45]. Although the rarest, most massive SMBHs at $z > 6$–7 could be explained by an origin from heavy seeds with sub-Eddington accretion, they still require continuous accretion over several hundred million years. The presence of overmassive black hole populations suggests the possibility that they could experience intermittent bursts of super-Eddington growth regardless of whether they originate from heavy or light seeds[45,46]. Super-Eddington accretion is likely to occur episodically, and the detection of LID-568 may represent one such episodic accretion phase. Future studies on a large sample of such objects will help to constrain the duty cycle of super-Eddington accretion and deepen our understanding of the mechanisms driving such high levels of accretion.

Methods

Parent sample

The parent sample comprised a previously undiscovered population of black holes, identified as near-IR-dropout X-ray sources (that is, invisible in the optical/near-IR bands) from the Chandra-COSMOS Legacy Survey[27,28], which consists of 4,016 X-ray sources over a large area of ~2.2 deg^2. We used the multiwavelength photometry from the most recent photometric catalogue from COSMOS2020[47] and HELP[48], containing GALEX FUV, NUV, CFHT U, Subaru/Hyper Suprime-Cam (HSC) g, r, i, z, y, UltraVISTA Y, H, J, Ks, Spitzer/Infrared Array Camera (IRAC) 3.6 μm, 4.5 μm, 5.8 μm, 8.0 μm, Spitzer/Multiband Imaging Photometer for Spitzer (MIPS) 24 μm, 70 μm, Herschel/Photodetector Array Camera and Spectrometer 100 μm, 160 μm and Herschel/Spectral and Photometric Imaging Receiver 250 μm, 350 μm, 500 μm photometry. We visually inspected all the optical/IR images and identified those without any optical counterparts within a 2″ radius, which corresponded to the uncertainty of the Chandra position. We excluded sources whose flux was contaminated by nearby bright sources and possible diffuse X-ray emission. This resulted in a final sample of 62 IR-dropout X-ray sources. All sources were detected in one or more of Spitzer/IRAC (3.6, 4.5, 5.8, 8.0 μm) bands and 26 sources were detected in Spitzer/MIPS 24 μm photometry. Ten sources had Herschel far-IR detections. None of these sources had a counterpart in the Very Large Array 3 GHz source catalogue[49].

ALMA observations

Spitzer/IRAC (ALMA) band 7 (275–373 GHz) continuum observations for all 62 IR-dropout X-ray sources were carried out in four observing blocks in November 2019 and January 2022 under the Cycle 7 programme 2019.1.01275.S (PI: Suh) with a total of 42 to 46 antennas. The observations were centred on the Chandra X-ray positions with an integration time of ~5 minutes per source. The data reduction was performed using the standard ALMA pipeline v.2021.2.0.128 (Common Astronomy Software Applications (CASA) v.6.2.1.7). We measured the integrated flux of all our targets using the imfit procedure from the CASA pipeline. The sources were modelled with a circular Gaussian profile of variable total flux, centroid, width, axis and position angle. The 870 μm flux of LID-568 was 545 ± 158 μJy, and the position of the 870 μm emission as measured from ALMA was in good agreement with those of Spitzer/IRAC. In Supplementary Fig. 1, we show multiband images of LID-568, which are invisible in the Subaru/HSC optical and UltraVISTA near-IR images.

JWST observations

We obtained JWST/NIRSpec[50,51] and MIRI/LRS[52] observations of LID-568 under the Cycle 1 GO programme number 1760 (PI: Suh). The NIRSpec/IFU observations were taken in April 2023 with the grating/filter combination of G395M/F290LP. This covered the spectral range of 3–5 μm with an average spectral resolution of $R \approx 1{,}000$. The field of view of the IFU mode was ~3″ × 3″, with each spatial element in the resulting IFU datacube of 0.1″ × 0.1″. We used the NRSIRS2 readout mode, which improves signal-to-noise ratio and reduces data volume. The observations were taken with 18 groups and one integration per exposure, using a four-point medium cycling dither pattern, resulting in a total exposure time of 1.45 h.

The NIRSpec/IFU data reduction was performed with the JWST Science Calibration pipeline v.1.11.4, using the CRDS context jwst_1149.pmap. We also added additional steps to improve the quality of the reduced data[53]. The reduction process consisted of three stages. The first stage accounted for detector-related issues, such as bias and dark subtraction, and cosmic ray flagging. At the end of this stage, the groups were fitted to create two-dimensional count rate images (that is, 'rate files'). The second stage applied the flat field correction, wavelength and flux calibration. The calibrated exposures were then processed in the third stage, where a further flagging of cosmic rays was applied before building the final datacube. Before running the second stage, we removed the detector low frequency noise $1/f$ affecting the rate files by subtracting from each spectral column its median value after applying a sigma clipping[54–56]. We fixed a pipeline bug reported by the STScI Helpdesk by setting all the saturated pixels and the pixels with bad flat field correction to 'DO_NOT_USE', which removes several outliers from the calibrated exposures. We removed the remaining outliers from the datacube by filtering out all the voxels with a jump over contiguous channels persisting for less than four channels, which is the typical width of these features. Finally, we subtracted the background as a function of the wavelength by calculating the median over ten spectra extracted from empty regions in the cube field of view in

each channel. We note that the background increases as a function of the wavelength, an expected effect due to an increase in the zodiacal and stray light[57]. We thus subtracted it channel by channel to obtain a background-free datacube.

The MIRI/LRS slit spectroscopy observations were conducted in January 2023 using a P750 disperser, covering a wavelength range of 5–12 μm with a spectral resolution of $R \approx 100$. The observations were performed with 360 groups per integration in FAST/FULL mode, with two integrations per exposure using a two-point dither along the slit. This resulted in a total exposure time of 1.1 h. The fully reduced data were retrieved from the Mikulski Archive for Space Telescope, which were processed using the JWST Science Calibration pipeline v.1.12.5, with the CRDS context jwst_1135.pmap.

X-ray luminosity

To compute the intrinsic X-ray luminosity in the 2–10 keV band, we used the XSpec software (v.12.13.0)[58] to fit the Chandra spectrum using a simple power-law model with the photon index fixed to $\Gamma = 1.9$, modified by both Galactic absorption ($N_H = 2.6 \times 10^{20}$ cm^{-2} (ref. 59)) and absorption at the redshift of the source, $N_H(z)$. The second absorption component accounted for both nuclear absorption due to the gas orbiting in the proximity of the SMBH (that is, torus) and absorption due to the interstellar medium in the host galaxy. The column density was measured as $\log N_H = 23.44$ (−0.34 + 0.47), and the absorption-corrected rest-frame 2–10 keV luminosity was determined as $\log (L_{2-10keV}) = 44.79$ (−0.33 + 0.27) (Supplementary Fig. 2).

To take into account the more complex absorption and reflection processes in the case of Compton-thick obscuration ($N_H > 10^{24}$ cm^{-2}), we also derived the column density and intrinsic X-ray luminosity using the MYtorus model[60,61]. This model consists of three components: the obscuration along the line of sight, including Compton scattering, applied to the primary power law, the reflection and the fluorescence emission line complex. The relative strength of these components was fixed to be the same, and the inclination angle between the line of sight and the axis of the torus was set to 75° to ensure interception of the obscuring torus. A power-law photon index of $\Gamma = 1.9$ was assumed. The column density and intrinsic X-ray luminosity derived from the MYtorus model were consistent with the standard power-law model, well in the Compton-thin regime. If we allowed the photon index to be a free parameter, the fit tended toward a softer power law ($\Gamma = 2.4$ for MYtorus and 2.9 for the simple power law) and, consequently, even higher column densities and intrinsic luminosities: $\log L_{2-10keV} = 45.08$ for MYtorus and 45.5 for the power law. Therefore, the choice of $\Gamma = 1.9$ was conservative in estimating intrinsic luminosity.

SED fitting

The SED fitting was performed using a modified approach based on ref. 62, utilizing the same SED libraries as those in AGNfitter[63]. Additionally, we independently fitted the SED using CIGALE[64] and X-CIGALE[65], the latter of which included the use of X-ray fluxes. Despite using various parametrizations and models for stellar populations, star formation history, dust emission and attenuation, and AGN emission from different SED fitting codes, we found that the SED of LID-568 shows an unusually red IR continuum that cannot be reproduced by any combination of the models and parameters used.

We further fitted the dust emission using the modified IR SED fitting code developed in ref. 32. We employed a composite mid-IR power law and two-temperature greybodies. We used a fixed value of the emissivity ($\beta = 1.5$), and allowed the mid-IR power-law slope (α) as a free parameter. The rest-frame observed photometric data (black) are presented alongside the best-fit IR SED (yellow) in the left panel of Extended Data Fig. 1. The SED is well fitted by a power law, and hot greybody (655.5 K) and warm greybody (71.5 K) components, which are much hotter than what is typically observed in star-forming galaxies (10–60 K). From the best fit, we derived the total IR luminosity ($L_{8-1,000\mu m}$) and the dust mass. In the right panel of Extended Data Fig. 1, we show the SED of LID-568 overlaid on the SED templates[66] of the AGN-dominated local ULIRG (Mrk 231), the extreme local starburst ULIRG (Arp 220) and the AGN dust torus model at redshift $z = 3.965$. The IR SED shape of LID-568 seems to be consistent with the torus model spectrum, but cannot be explained by currently available IR SED templates of obscured AGN/ULIRGs.

AGN bolometric luminosity

The bolometric luminosity of AGNs can be estimated from the X-ray luminosity by applying a suitable bolometric correction[67]. To accurately estimate the total intrinsic luminosity radiated by the AGN accretion disc, it is necessary to constrain the absorption-corrected intrinsic X-ray luminosity, as X-rays are often obscured and may include reprocessed radiation. The AGN bolometric luminosity of $L_{bol} = 46.59$ erg s^{-1} is derived using the absorption-corrected rest-frame 2–10 keV luminosity by applying a luminosity-dependent bolometric correction as described in ref. 67.

We also computed the AGN luminosity from the SED by integrating absorption-corrected total X-ray luminosity ($L_{0.1-100keV}$) and the best-fit AGN torus luminosity ($L_{1-1,000\mu m}$) following ref. 62. To convert the IR luminosity into a proxy for the intrinsic nuclear luminosity, we considered the geometry of the torus and its orientation by applying the following correction factors: the first correction is related to the covering factor, which represents the fraction of the primary UV-optical radiation intercepted by the torus (~1.5 (ref. 68)) and the second correction is due to the anisotropy of the IR dust emission, which is a function of the viewing angle (~1.3 (ref. 69)). The derived AGN bolometric luminosity was $L_{bol} = 46.68$ erg s^{-1}, which is consistent with the X-ray-derived bolometric luminosity.

We additionally derived the bolometric luminosity using the Hα luminosity following ref. 18. We calculated the rest-frame 5,100 Å luminosity from Hα luminosity using the equation in ref. 70. The bolometric luminosity was estimated using the bolometric correction factor in ref. 71, $L_{bol} = 10.33 \times L_{5,100}$, to be 45.60 erg s^{-1}, which is ~1 dex lower than that derived from other methods (that is, X-ray luminosity and SED fitting). This indicates that the Hα emission could possibly be highly obscured, potentially leading to an underestimate of the Hα-derived black hole mass by a factor of a few. However, we point out that when estimating the Eddington ratio using an internally consistent method based on the Hα emission for both AGN bolometric luminosity and the black hole mass, the black hole is still accreting at the super-Eddington accretion level of ~4.4. We note that the bolometric correction factor for Hα luminosity could be uncertain for those obscured AGNs with super-Eddington accretion at high redshifts. The estimated bolometric luminosities obtained using various methods are shown in Supplementary Fig. 3.

Black hole mass and outflows

The single-epoch virial black hole mass was estimated using the broad Hα emission line width and the line luminosity from the rest-frame UV/optical spectra as a proxy for the characteristic velocity and the size of the BLR. The NIRSpec spectra were extracted from a circular aperture centred at the position of the BLR, with radius of 0.2″ ($r = 2$ pix). We utilized the mpfit routine for fitting the emission lines, employing a Levenberg–Marquardt least-squares minimization algorithm to derive the best-fit parameters and assess the overall fit quality[72]. Specifically, we fitted and subtracted a power-law continuum (f_λ) as a function of wavelength (λ), $f_\lambda \propto \lambda^{-a}$, from the spectra and performed a simultaneous fit with a combination of multiple narrow and broad Gaussian components to best characterize the line shape. For the narrow emission lines, we fitted the [N II] 6,548, 6,583 Å lines with a fixed ratio of 2.96, as well as the [S II] 6,716, 6,731 Å doublet, along with Hα 6,563 Å. We constrained the line widths and relative line centres of the narrow-line components to the narrow Hα emission line. The broad Hα line was best fit with two

broad Gaussian components: one for the BLR and the other for the blue-shifted outflow component. We also included blue-shifted broad Gaussian components for the [S II] 6,716, 6,731 Å doublet.

Additionally, we investigated the inclusion of additional broad Gaussian components for the [N II] 6,548, 6,583 Å lines as outflow components. We also tested the fit both with and without constraining the range of ratios of the [S II] 6,716, 6,731 Å doublet. However, we found no meaningful statistical improvement from adding these broad Gaussian components. For the former, this lack of meaningful improvement in the fit is likely to be due to the [N II] components being overwhelmed by the much stronger Hα emission. For the latter, the blueward [S II] emission appears to dominate the fit in that spectral region, and, given the lower signal-to-noise ratio of both features, it is not surprising that a similar goodness of fit is returned by forcing the ratio of the strength of the two components within the canonical allowable range. Furthermore, changes in the fitting approach did not appreciably affect the inferred black hole mass beyond the inherent random and systematic uncertainties.

Finally, we measured the broad-line width and the line luminosity from the best-fit spectra. The black hole mass was computed using the equation from ref. 70. Although the measurement uncertainties on M_{BH} were relatively small (~0.1 dex), systematic uncertainties associated with different single-epoch virial calibrations carried a scatter of ~0.3 dex (refs. 35,36,73). We estimated the black hole mass to be $7.2\ (-5.4 + 10.8) \times 10^6\ M_\odot$. The uncertainties of the black hole mass were determined by the sum of the statistical and intrinsic scatter of the calibrations.

Extended Data Fig. 2 (left) shows the best-fit model around the Hα, [N II] and [S II] region. Broadened and/or shifted components in emission lines trace gas with different kinematics, potentially indicating outflows. We investigated possible signs of outflows using Hα and [S II] lines because [O III], which typically serves as a tracer of outflows, is not covered by our dataset. In Extended Data Fig. 2 (right), we compare the blue-shifted Hα emission line with that of the [S II] line components. Although we left the line widths and relative line centres of the blue-shifted components as free parameters, the broad blue-shifted emission is evident in both the Hα and [S II] lines, exhibiting the same broad-line width and velocity offsets, which suggests that they are kinematically coupled. From the best-fit model, we inferred a spatially unresolved outflow velocity of ~−540 km s^{-1}. Similar velocities are associated with the spatially extended Hα emission (Extended Data Fig. 3), which could be part of the outflow or indicate ongoing merger activity. The mass of the ionized outflow as inferred from the blue-shifted outflow component of the broad Hα emission was $1.4 \times 10^7\ M_\odot$ using equation (1) from ref. 74. Assuming an outflow velocity of −540 km s^{-1} and that the extended Hα emission is representative of the outflow radius (that is, $r_{out} = 1''$ (~7 kpc)), the outflow rate was ~$3.1\ M_\odot\ yr^{-1}$.

Environment

We measured the environmental density surrounding LID-568 by employing the Voronoi tessellation Monte Carlo mapping described in refs. 75,76. Briefly, this technique uses a weighted combination of spectroscopic and photometric redshifts to construct a galaxy overdensity cube in thin (7.5 proper Mpc) slices running from $2 < z < 5$. The mapping leverages the wealth of panchromatic imaging data from COSMOS, as well as a large number of spectroscopic redshifts drawn from public surveys and proprietary data. The particular instance of the Voronoi tessellation Monte Carlo mapping used in this work was identical to that of ref. 77.

After an overdensity cube had been constructed over the full redshift range, a source extractor-based post-processing technique, as described in ref. 76, was used to link detections of overdensities across contiguous slices to search for coherent structure and estimate the mass of the detected structure. For density mapping at $z > 2$, this post-processing technique was trained on mock observations of custom-built light cones to maximize the purity and completeness associated with the detection of protogroups and protoclusters. At the spatial location of LID-568, the spectroscopic coverage in the COSMOS field was fairly sparse, and we estimated that our method was >50% complete only for structures with $z = 0$ masses greater than $10^{14.5}\ M_\odot$, that is, massive protoclusters, at $z \approx 4$.

We find no evidence that LID-568 is associated with an overdensity of galaxies. The local overdensity at the location of LID-568 was $\log(1 + \delta_{gal}) = 0.11$, which is approximately a 1σ fluctuation over the mean (galaxy) density of the universe at these redshifts. Measuring the average overdensity in a cylindrical aperture of radius 1 proper Mpc and depth of $\Delta z = 0.02$ centred on the redshift of LID-568 recovered a consistent value. Additionally, we detected no associated coherent structure within $\Delta z = 0.04$ and $R < 5$ proper Mpc of LID-568, which indicates that it is not likely to be embedded in a massive forming cluster. However, given the paucity of spectroscopic redshifts in proximity to LID-568, we cannot rule out membership in a lower mass structure. We also note that, at such redshifts, galaxy-traced methods can fail to detect massive overdensities that are well traced by neutral hydrogen[78]. Future spectroscopic observations of the surroundings of LID-568 and similar sources will help to better quantify the environments in which they reside.

Data availability

The data for ALMA and JWST used in this study are publicly available through their respective data archives. These observations are associated with the JWST GO programme no. 1760 and the ALMA programme no. 2019.1.01275.S. Other data generated and/or analysed during the study are available from the corresponding author upon reasonable request.

References

1. Mortlock, D. J. et al. A luminous quasar at a redshift of $z = 7.085$. *Nature* **474**, 616 (2011).
2. Bañados, E. et al. An 800-million-solar-mass black hole in a significant neutral Universe at a redshift of 7.5. *Nature* **553**, 473 (2018).
3. Yang, J. et al. Probing early supermassive black hole growth and quasar evolution with near-infrared spectroscopy of 37 reionization-era quasars at $6.3 < z < 7.64$. *Astrophys. J.* **923**, 262 (2021).
4. Wang, F. et al. A luminous quasar at redshift 7.642. *Astrophys. J.* **907**, 1 (2021).
5. Farina, E. P. et al. The X-shooter/ALMA sample of quasars in the epoch of reionization. II. Black hole masses, Eddington ratios, and the formation of the first quasars. *Astrophys. J.* **941**, 106 (2022).
6. Fan, X., Bañados, E. & Simcoe, R. A. Quasars and the intergalactic medium at cosmic dawn. *Annu. Rev. Astron. Astrophys.* **61**, 373 (2023).
7. Rees, M. F. Quasars. *Observatory* **98**, 210 (1978).
8. Volonteri, M. The formation and evolution of massive black holes. *Science* **337**, 544 (2012).
9. Natarajan, P. Seeds to monsters: tracing the growth of black holes in the universe. *Gen. Relativ. Gravit.* **46**, 1702 (2014).
10. Volonteri, M. & Rees, M. J. Rapid growth of high-redshift black holes. *Astrophys. J.* **633**, 624 (2005).
11. Smith, B. D. et al. The growth of black holes from Population III remnants in the Renaissance simulations. *Mon. Not. R. Astron. Soc.* **480**, 3762 (2018).
12. Volonteri, M., Lodato, G. & Natarajan, P. The evolution of massive black hole seeds. *Mon. Not. R. Astron. Soc.* **383**, 1079 (2008).
13. Natarajan, P. et al. Unveiling the first black holes with JWST: multi-wavelength spectral predictions. *Astrophys. J.* **838**, 117 (2017).

14. Volonteri, M., Habouzit, M. & Colpi, M. The origins of massive black holes. *Nat. Rev. Phys* **3**, 732 (2021).
15. Kashlinsky, A. LIGO gravitational wave detection, primordial black holes, and the near-IR cosmic infrared background anisotropies. *Astrophys. J. Lett.* **823**, 25 (2016).
16. Hasinger, G. Illuminating the dark ages: cosmic backgrounds from accretion onto primordial black hole dark matter. *J. Cosmol. Astropart. Phys.* **07**, 022 (2020).
17. Cappelluti, N., Hasinger, G. & Natarajan, P. Exploring the high-redshift PBH-ΛCDM Universe: early black hole seeding, the first stars and cosmic radiation backgrounds. *Astrophys. J.* **926**, 205 (2022).
18. Harikane, Y. et al. A JWST/NIRSpec first census of broad-line AGNs at z=4–7: detection of 10 faint AGNs with M_{BH}=10^6–10^8 $M_\odot$ and their host galaxy properties. *Astrophys. J.* **959**, 39 (2023).
19. Kocevski, D. D. et al. Hidden little monsters: spectroscopic identification of low-mass, broad-line AGNs at z>5 with CEERS. *Astrophys. J.* **954**, 4 (2023).
20. Maiolino, R., et al. JADES. The diverse population of infant black holes at 4<z<11: merging, tiny, poor, but mighty. Preprint at https://arxiv.org/abs/2308.01230 (2023)
21. Übler, H. et al. GA-NIFS: a massive black hole in a low-metallicity AGN at z~5.55 revealed by JWST/NIRSpec IFS. *Astron. Astrophys.* **677**, 145 (2023).
22. Furtak, L. J. et al. A high black-hole-to-host mass ratio in a lensed AGN in the early Universe. *Nature* **628**, 57 (2024).
23. Greene, J. E. et al. UNCOVER spectroscopy confirms the surprising ubiquity of active galactic nuclei in red sources at z>5. *Astrophys. J.* **964**, 39 (2024).
24. Matthee, J. et al. Little red dots: an abundant population of faint active galactic nuclei at z~5 revealed by the EIGER and FRESCO JWST surveys. *Astrophys. J.* **963**, 129 (2024).
25. Pacucci, F., Nguyen, B., Carniani, S., Maiolino, R. & Fan, X. JWST CEERS and JADES active galaxies at z=4–7 violate the local $M_\bullet$–$M_\star$ relation at >3σ: implications for low-mass black holes and seeding models. *Astrophys. J.* **957**, 3 (2003).
26. Kocevski, D. D., et al. The rise of faint, red AGN at z>4: a sample of little red dots in the JWST extragalactic legacy fields. Preprint at https://arxiv.org/abs/2404.03576 (2024).
27. Civano, F. et al. The *Chandra* COSMOS Legacy survey: overview and point source catalog. *Astrophys. J.* **819**, 62 (2016).
28. Marchesi, S. et al. The *Chandra* COSMOS Legacy survey: optical/IR identifications. *Astrophys. J.* **817**, 34 (2016).
29. Pognan, Q., Trakhtenbrot, B., Sbarrato, T., Schawinski, K. & Bertemes, C. Searching for super-Eddington quasars using a photon trapping accretion disc model. *Mon. Not. R. Astron. Soc.* **492**, 4058 (2020).
30. Done, C., Davis, S. W., Jin, C., Blaes, O. & Ward, M. Intrinsic disc emission and the soft X-ray excess in active galactic nuclei. *Mon. Not. R. Astron. Soc.* **420**, 1848 (2012).
31. Tang, J.-J. et al. Rapid black hole growth at the dawn of the Universe: a super-Eddington quasar at z=6.6. *Mon. Not. R. Astron. Soc.* **484**, 2575 (2019).
32. Casey, C. M. Far-infrared spectral energy distribution fitting for galaxies near and far. *Mon. Not. R. Astron. Soc.* **425**, 3094 (2012).
33. Xiao, M.-Y. et al. The hidden side of cosmic star formation at z>3: bridging optically dark and Lyman-break galaxies with GOODS-ALMA. *Astron. Astrophys.* **672**, A18 (2023).
34. Gentile, F. et al. Illuminating the dark side of Cosmic star formation. III. Building the largest homogeneous sample of radio-selected dusty star-forming galaxies in COSMOS with PhoEBO. *Astrophys. J.* **962**, 26 (2024).
35. Du, P. et al. Supermassive black holes with high accretion rates in active galactic nuclei. V. A new size-luminosity scaling relation for the broad-line region. *Astrophys. J.* **825**, 126 (2016).
36. GRAVITY Collaboration et al. The size-luminosity relation of local active galactic nuclei from interferometric observations of the broad-line region. *Astron. Astrophys.* **684**, 167 (2024).
37. Soltan, A. Masses of quasars. *Mon. Not. R. Astron. Soc.* **200**, 115 (1982).
38. Martini, P. & Weinberg, D. H. Quasar clustering and the lifetime of quasars. *Astrophys. J.* **547**, 12 (2001).
39. Lupi, A., Quadri, G., Volonteri, M., Golpi, M. & Regan, J. A. Sustained super-Eddington accretion in high-redshift quasars. *Astron. Astrophys.* **686**, 256 (2024).
40. Hopkins, P. F., Hernquist, L., Cox, T. J. & Kereš, D. A cosmological framework for the co-evolution of quasars, supermassive black holes, and elliptical galaxies. I. Galaxy mergers and Quasar activity. *Astrophys. J. Suppl.* **175**, 356 (2008).
41. Mezcua, M. et al. Overmassive black holes in dwarf galaxies out to z~0.9 in the VIPERS survey. *Astrophys. J. Lett.* **943**, 5 (2023).
42. Elvis, M., Marengo, M. & Karovska, M. Smoking quasars: a new source for cosmic dust. *Astrophys. J.* **567**, 107 (2002).
43. Regan, J. A. et al. Super-Eddington accretion and feedback from the first massive seed black holes. *Mon. Not. R. Astron. Soc.* **486**, 3892 (2019).
44. Massonneau, W., Volonteri, M., Dubois, Y. & Beckmann, R. S. How the super-Eddington regime regulates black hole growth in high-redshift galaxies. *Astron. Astrophys.* **670**, A180 (2023).
45. Volonteri, M., Silk, J. & Dubus, G. The case for supercritical accretion onto massive black holes at high redshift. *Astrophys. J.* **804**, 148 (2015).
46. Juodžbalis, I. et al. A dormant, overmassive black hole in the early universe. Preprint at https://arxiv.org/abs/2403.03872 (2024).
47. Weaver, J. R. et al. COSMOS2020: a panchromatic view of the Universe to z~10 from two complementary catalogs. *Astrophys. J. Suppl.* **258**, 11 (2022).
48. Shirley, R. et al. HELP: the herschel extragalactic legacy project. *Mon. Not. R. Astron. Soc.* **507**, 129 (2021).
49. Smolčić, V. et al. The VLA-COSMOS 3 GHz Large Project: continuum data and source catalog release. *Astron. Astrophys.* **602**, 1 (2017).
50. Jakobsen, P. et al. The Near-Infrared Spectrograph (NIRSpec) on the James Webb Space Telescope. I. Overview of the instrument and its capabilities. *Astron. Astrophys.* **661**, 80 (2022).
51. Böker, T. et al. The Near-Infrared Spectrograph (NIRSpec) on the James Webb Space Telescope. III. Integral-field spectroscopy. *Astron. Astrophys.* **661**, 82 (2022).
52. Kendrew, S. et al. The mid-infrared instrument for the James Webb Space Telescope, IV: the low-resolution spectrometer. *Publ. Astron. Soc. Pac.* **127**, 623 (2015).
53. Loiacono, F. et al. A quasar-galaxy merger at z~6.2: black hole mass and quasar properties from the NIRSpec spectrum. *Astron. Astrophys.* **685**, 121 (2024).
54. Kashino, D. et al. EIGER. I. A large sample of [O III]-emitting galaxies at 5.3<z<6.9 and direct evidence for local reionization by galaxies. *Astrophys. J.* **950**, 66 (2023).
55. Perna, M. et al. GA-NIFS: the ultra-dense, interacting environment of a dual AGN at z~3.3 revealed by JWST/NIRSpec IFS. *Astron. Astrophys.* **679**, 89 (2023).
56. Rauscher, B. J. NSClean: an algorithm for removing correlated noise from JWST NIRSpec images. *Publ. Astron. Soc. Pac.* **136**, 015001 (2024).
57. Rigby, J. et al. The science performance of JWST as characterized in commissioning. *Publ. Astron. Soc. Pac.* **135**, 8001 (2023).
58. Arnaud, K. A. XSPEC: the first ten years. *Astron. Data Anal. Softw. Syst.* **101**, 17 (1996).
59. Kalberia, P. M. W. et al. The Leiden/Argentine/Bonn (LAB) Survey of Galactic HI. Final data release of the combined LDS and IAR surveys with improved stray-radiation corrections. *Astron. Astrophys.* **440**, 775 (2005).

60. Murphy, K. D. & Yaqoob, T. An X-ray spectral model for Compton-thick toroidal reprocessors. *Mon. Not. R. Astron. Soc.* **397**, 1549 (2009).
61. Lanzuisi, G. et al. The Chandra COSMOS Legacy Survey: Compton-thick AGN at high redshift. *Mon. Not. R. Astron. Soc.* **480**, 2578 (2018).
62. Suh, H. et al. Multi-wavelength properties of type 1 and type 2 AGN host galaxies in the Chandra-COSMOS Legacy Survey. *Astrophys. J.* **872**, 168 (2019).
63. Calistro Rivera, G., Lusso, E., Hennawi, J. F. & Hogg, D. W. AGNfitter: a Bayesian MCMC approach to fitting spectral energy distribution of AGNs. *Astrophys. J.* **833**, 98 (2016).
64. Boquien, M. et al. CIGALE: a python Code Investigating GALaxy Emission. *Astron. Astrophys.* **622**, 103 (2019).
65. Yang, G. et al. X-CIGALE: fitting AGN/galaxy SEDs from X-ray to infrared. *Mon. Not. R. Astron. Soc.* **491**, 740 (2020).
66. Polletta, M. et al. Spectral energy distributions of hard X-ray selected active galactic nuclei in the XMM-Newton medium deep survey. *Astrophys. J.* **663**, 81 (2007).
67. Marconi, A. et al. Local supermassive black holes, relics of active galactic nuclei and the X-ray background. *Mon. Not. R. Astron. Soc.* **351**, 169 (2004).
68. Gilli, R., Comastri, A. & Hasinger, G. The synthesis of the cosmic X-ray background in the Chandra and XMM-Newton era. *Astron. Astrophys.* **463**, 79 (2007).
69. Lusso, E. et al. The bolometric output and host-galaxy properties of obscured AGN in the XMM-COSMOS survey. *Astron. Astrophys.* **534**, 110 (2011).
70. Greene, J. E. & Ho, L. C. Estimating black hole masses in active galaxies using the Hα emission line. *Astrophys. J.* **630**, 122 (2005).
71. Richards, G. T. et al. Spectral energy distributions and multiwavelength selection of type 1 quasars. *Astrophys. J. Suppl.* **166**, 470 (2006).
72. Suh, H. et al. No significant evolution of relations between black hole mass and galaxy total stellar mass up to $z\sim2.5$. *Astrophys. J.* **889**, 32 (2020).
73. Trakhtenbrot, B. & Netzer, H. Black hole growth to $z=2-$ I. Improved virial methods for measuring M_{BH} and L/L_{Edd}. *Mon. Not. R. Astron. Soc.* **427**, 1096 (2012).
74. Cresci, G. et al. Bubbles and outflows: the novel JWST/NIRSpec view of the $z=1.59$ obscured quasar XID2028. *Astron. Astrophys.* **672**, 128 (2023).
75. Lemaux, B. C. et al. The VIMOS Ultra-Deep Survey: emerging from the dark, a massive proto-cluster at $z\sim4.57$. *Astron. Astrophys.* **615**, 77 (2018).
76. Hung, D. et al. Establishing a new technique for discovering large-scale structure using the ORELSE survey. *Mon. Not. R. Astron. Soc.* **491**, 5524 (2020).
77. Lemaux, B. C. et al. The VIMOS Ultra Deep Survey: the reversal of the star-formation rate – density relation at $2<z<5$. *Astron. Astrophys.* **662**, 33 (2022).
78. Newman, A. B. et al. A population of ultraviolet-dim protoclusters detected in absorption. *Nature* **606**, 475 (2022).

Acknowledgements

H.S., J.S., E.P.F., B.C.L., M.R. and D.H. are supported by the international Gemini Observatory, a program of NSF NOIRLab, which is managed by the Association of Universities for Research in Astronomy (AURA) under a cooperative agreement with the National Science Foundation, on behalf of the Gemini partnership of Argentina, Brazil, Canada, Chile, the Republic of Korea and the United States. F.L. acknowledges support from the INAF 2023 mini-grant 'Exploiting the powerful capabilities of JWST/NIRSpec to unveil the distant Universe'. M.M. acknowledges support from the Spanish Ministry of Science and Innovation through the project PID2021-124243NB-C22. This work was partially supported by the programme Unidad de Excelencia María de Maeztu CEX2020-001058-M. S.K.Y. acknowledges support from the Korean National Research Foundation (2020R1A2C3003769, 2022R1A6A1A03053472) and the IBS computing centre for the super-Eddington accretion project. This work is based on observations made with the NASA/ESA/CSA JWST. The data were obtained from the Mikulski Archive for Space Telescopes at the Space Telescope Science Institute, which is operated by the Association of Universities for Research in Astronomy, Inc., under NASA contract NAS 5-03127 for JWST. These observations are associated with programme no. 1760. Support for programme no. 1760 was provided by NASA through a grant from the Space Telescope Science Institute, which is operated by the Association of Universities for Research in Astronomy, Inc., under NASA contract NAS 5-03127. This paper makes use of the following ALMA data: ADS/JAO.ALMA#2019.1.01275.S. ALMA is a partnership of ESO (representing its member states), NSF (United States) and NINS (Japan), together with NRC (Canada), MOST and ASIAA (Taiwan), and KASI (Republic of Korea), in cooperation with the Republic of Chile. The Joint ALMA Observatory is operated by ESO, AUI/NRAO and NAOJ. The National Radio Astronomy Observatory is a facility of the National Science Foundation operated under cooperative agreement by Associated Universities, Inc.

Author contributions

H.S. was the principal investigator of the JWST and ALMA proposals, led the analysis and interpretation of the results, and drafted the paper. H.S. and G.H. performed the sample selection. J.S. contributed to the analysis of the JWST NIRSpec IFU data and the interpretation of the results. F.L. reduced the JWST NIRSpec IFU data and wrote the relevant section. G.L. and S.M. analysed the X-ray data and wrote the relevant section. B.C.L. and D.H. performed all analysis relating to the environment and B.C.L. wrote the relevant section. S.K.Y. and S.H. performed simulations and provided discussions on black hole growth. E.P.F., M.M., R.D. and M.V. helped with the interpretation of the results and provided comments on the analysis. All authors contributed to the discussion of the presented results and the preparation of the paper.

Competing interests

The authors declare no competing interests.

Additional information

Extended data is available for this paper at https://doi.org/10.1038/s41550-024-02402-9.

Supplementary information The online version contains supplementary material available at https://doi.org/10.1038/s41550-024-02402-9.

Correspondence and requests for materials should be addressed to Hyewon Suh.

Peer review information *Nature Astronomy* thanks John Regan and the other, anonymous, reviewer(s) for their contribution to the peer review of this work.

[1]International Gemini Observatory/NSF NOIRLab, Hilo, HI, USA. [2]INAF - Osservatorio di Astrofisica e Scienza dello Spazio di Bologna, Bologna, Italy. [3]Institute of Nuclear and Particle Physics, TU Dresden, Dresden, Germany. [4]DESY, Hamburg, Germany. [5]Deutsches Zentrum für Astrophysik, Görlitz, Germany. [6]Department of Physics and Astronomy, Clemson University, Clemson, SC, USA. [7]Dipartimento di Fisica e Astronomia (DIFA) Augusto Righi, Università di Bologna, Firenze, Italy. [8]Institute of Space Sciences (ICE, CSIC), Campus UAB, Carrer de Magrans, Spain. [9]Institut d'Estudis Espacials de Catalunya (IEEC), Edifici RDIT, Campus UPC, Castelldefels, Spain. [10]Department of Physics and Astronomy, University of California, Davis, Davis, CA, USA. [11]Institut d'Astrophysique de Paris (UMR 7095: CNRS & Sorbonne Universite), Paris, France. [12]NASA Goddard Space Flight Center, Greenbelt, MD, USA. [13]Department of Astronomy and Yonsei University Observatory, Yonsei University, Seoul, Republic of Korea. ✉e-mail: hyewon.suh@noirlab.edu

https://doi.org/10.1038/s41550-024-02402-9

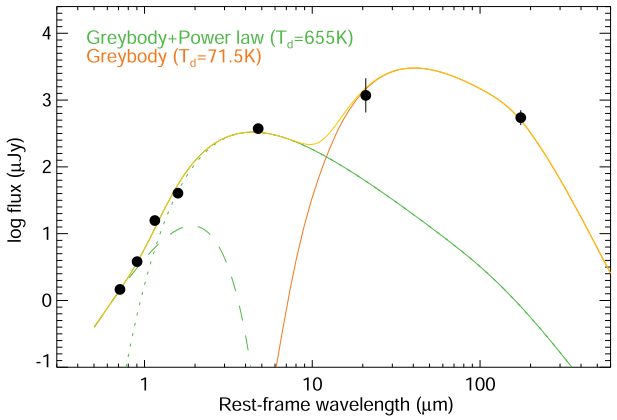

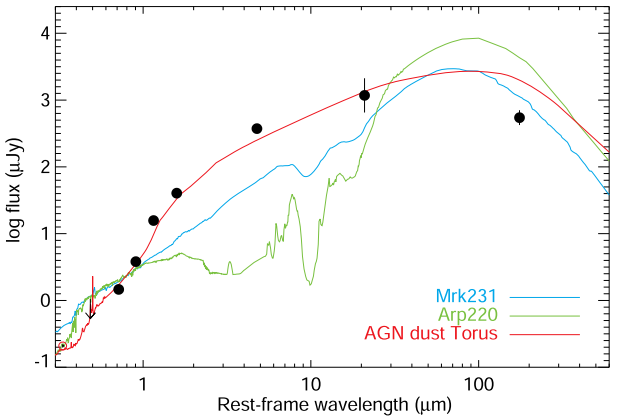

Extended Data Fig. 1 | SED fit. Left: the rest-frame observed photometric data (black) with 1σ uncertainties, along with the best-fit model (yellow). The model includes a power-law (green dashed), a hot greybody (655 K; green dotted), and a warm greybody (71 K; orange) components. Right: Overlay of the observed data (black) with the SED templates[61] of the AGN-dominated local ULIRG (Mrk 231), the extreme local starburst ULIRG (Arp 220), and the AGN dust torus model at redshift z = 3.965.

https://doi.org/10.1038/s41550-024-02402-9

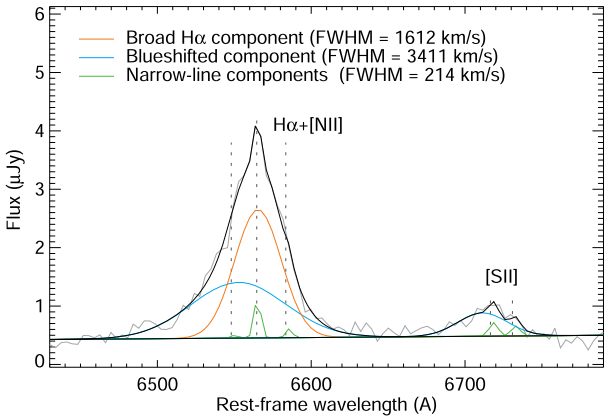

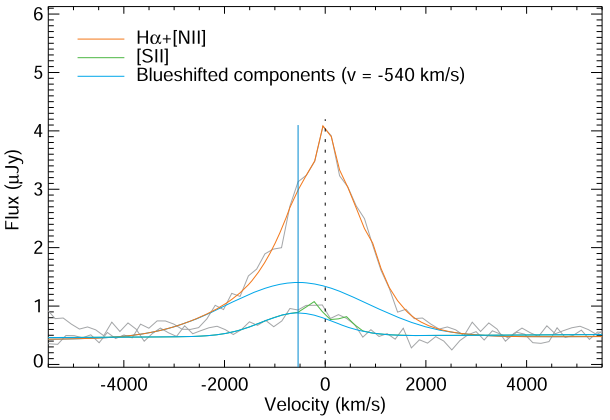

Extended Data Fig. 2 | Hα broad-line fitting. Left: The JWST NIRSpec spectrum (grey) with the best-fit model (black). The spectrum is extracted from a circular aperture of radius 0.2″ centered on the central broad-line region. The power-law continuum (black), narrow-line components (green), broad-line components (orange), and outflow components (blue) are indicated. Dotted vertical lines mark the line centers of the narrow-line components. Right: Comparison of the blue-shifted (outflow) line profiles of the Hα + [NII] and [SII] in velocity space. The blue-shifted (outflow) components are observed at a velocity of ~−540 km/s relative to systemic.

https://doi.org/10.1038/s41550-024-02402-9

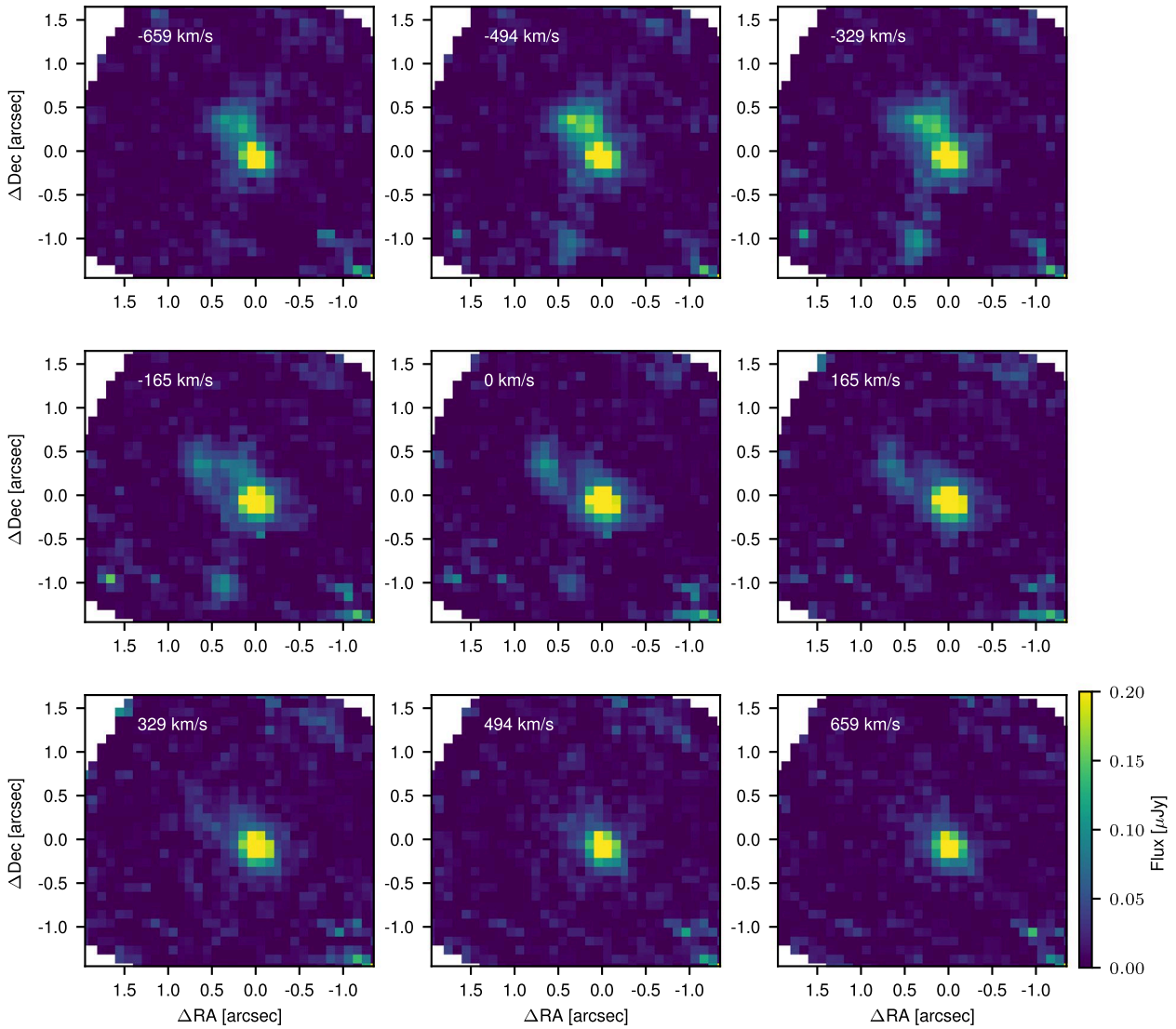

Extended Data Fig. 3 | JWST NIRSpec/IFU channel maps for the Hα emission around LID-568. Each map was created by averaging 3 neighboring channels. The maps are shown in single-channel steps corresponding to velocity steps of 165 km/s. The velocity marked in each map indicates the central velocity of the 3-channel average relative to the 0 km/s map centered at 3.259 μm. Spatial offsets in arcseconds are shown relative to the AGN location.